

Local current transport and surface potential of photovoltaic Cu(In,Ga)Se₂ thin films probed by multi-scale imaging methods

This content has been downloaded from IOPscience. Please scroll down to see the full text.

2013 Adv. Nat. Sci: Nanosci. Nanotechnol. 4 015007

(<http://iopscience.iop.org/2043-6262/4/1/015007>)

View [the table of contents for this issue](#), or go to the [journal homepage](#) for more

Download details:

IP Address: 203.255.172.21

This content was downloaded on 08/09/2016 at 08:16

Please note that [terms and conditions apply](#).

You may also be interested in:

[Effect of substrate temperature on the structural and electrical properties of CIGS films](#)

H Wang, Y Zhang, X L Kou et al.

[Optimizing Ga-profiles for highly efficient Cu\(In, Ga\)Se₂ thin film solar cells in simple and complex defect models](#)

C Frisk, C Platzer-Björkman, J Olsson et al.

[Nanoscale investigation of charge transport at the grain boundaries and wrinkles in graphene film](#)

Muneer Ahmad, Hyosub An, Yong Seung Kim et al.

[Surface photovoltage analysis of thin CdS layers on polycrystalline chalcopyrite absorberlayers by Kelvin probe force microscopy](#)

Th Glatzel, M Rusu, S Sadewasser et al.

[Advances in AFM for the electrical characterization of semiconductors](#)

Rachel A Oliver

[The role of growth temperature and Se flux on Cu\(In,Ga\)Se₂ thin film deposited on a stainless steel substrate and solar cell](#)

Boyan Li, Yi Zhang, Biao Wang et al.

Local current transport and surface potential of photovoltaic Cu(In, Ga)Se₂ thin films probed by multi-scale imaging methods*

A R Jeong¹, G Y Kim¹, W Jo¹, D H Nam², H Cheong², H J Jo³, D-H Kim³, S J Sung³, J K Kang³ and D H Lee³

¹ Department of Physics, Ewha Womans University, Seoul 120-750, Republic of Korea

² Department of Physics, Sogang University, Seoul 121-742, Republic of Korea

³ Daegu Gyeongbuk Institute of Science and Technology, Daegu 711-873, Republic of Korea

E-mail: wmjo@ewha.ac.kr

Received 13 October 2012

Accepted for publication 31 December 2012

Published 29 January 2013

Online at stacks.iop.org/ANSN/4/015007

Abstract

Microstructural alteration induces non-uniform device characteristics in polycrystalline thin films. In thin-film solar cells based on Cu(In, Ga)Se₂ (CIGS), local electrical properties are investigated by Raman scattering spectroscopic imaging and scanning probe microscopic tools. Localized and uneven intensity of phonon modes, which represent different orientation and phases, elucidate the nature of non-uniformity of crystallinity, composition and defects in the films. Surface potential mapping at nanoscale is performed by Kelvin probe force microscopy, showing ~40 mV of band-bending at the grain boundaries. Externally biased-current mapping, which is obtained by conductive atomic force microscopy, shows preferred current path in the films.

Keywords: Cu(In, Ga)Se₂, thin-films, solar cells, surface current and potential, atomic force microscopy

Classification number: 4.10

1. Introduction

Thin-film solar cells based on Cu(In, Ga)Se₂ (CIGS) have been extensively developed and are being considered for commercialization [1–3]. However, the market is still mostly incentive-driven and not yet urged by profit. CIGS solar cells manufactured by the three-stage co-evaporation process have achieved a record high efficiency of ~20% [4]. In any process, a high-quality absorber layer is a basic requirement for fabricating the highly efficient solar cells [1, 4–6]. Vexingly, the difficulty with large scale-up and uniform growth of the CIGS films hinders commercial manufacturing.

Thus, a new process for developing large-area substrates at relatively low cost is demanded, while developing an understanding of all the possible defects and the charge transport mechanism is now being revisited by many research groups. The multi-scale nature of the defects in CIGS materials requires systematic endeavors to elucidate their physical properties over a wide range of length scales. In particular, although the grain boundaries (GBs) in CIGS thin films are known to assist in electron–hole separation, we still lack an understanding of the mechanism at the nanoscale or microscale [7–13]. A graded distribution of the elements through the materials and complicated point defects have been introduced by depth-profile studies, while surface analysis has been conducted by atomic force microscopy. Complementary studies using optical tools and surface scanning probes as well as conventional electron microscopy will enrich

* Invited talk at the 6th International Workshop on Advanced Materials Science and Nanotechnology IWAMSN2012, 30 October–2 November 2012, Ha Long, Vietnam.



our knowledge of the microstructure and charge transport mechanism. This will eventually allow us to increase the efficiencies of CIGS solar cells to up to 26%, which is believed to be the practical limit at the moment.

In this paper, we present the optical and electrical properties of CIGS thin-films in the form of images and maps ranging from the microscale to the nanoscale. Integration of the spectroscopic response on the CIGS films characterized by Raman scattering spectroscopy allows us to extend our scrutiny from the distribution of phonon modes of the crystallites to inhomogeneous growth of pure chalcopyrite phases. Comparing this information with scanning electron micrographs, it is likely that GBs, being micro dimensional defects, are correlated to the Raman responses. For narrowing down the scale to the submicron level, we need a scanning probe tool equipped with metal-coated cantilevers: Kelvin probe force microscopy (KPFM) and conductive atomic force microscopy (CAFM) for surface potential and current, respectively. Measurements with KPFM provide an understanding of the electrostatic properties of GBs and are used to determine the band diagrams across GBs [14]. Our data suggest that the enhanced efficiency of solar cells results from significant mobility and carrier separation by the electric current and potential gradient at the GBs. From these multi-scale measurements, we can ensure the distribution of polycrystalline CIGS properties, which will aid our understanding of the characteristics needed for optimum photovoltaic performance.

2. Experiment

CIGS films were prepared by a co-evaporation process developed specifically for optimal cell efficiencies [15–17]. In the first step, three sources of In, Ga and Se were deposited on 1 μm -thick Mo on a soda lime glass at a substrate temperature of 420 °C. Cu and Se fluxes were then evaporated to the as-grown In–Ga–Se layer at a substrate temperature of 550 °C, consequently the layer was transformed to a Cu-rich Cu–In–Ga–Se film. In the last step, a small amount of In, Ga and Se was added to the Cu-rich Cu–In–Ga–Se layer at 550 °C. The final composition of the grown film was Ga/(Ga+In) \sim 0.3 and there is a compositional groove throughout the layer. The substrate temperature was measured from the back of the substrate with an infrared pyrometer and the deposition rate was measured using a quartz crystal microbalance. The thickness of the grown films was \sim 2 μm . From this process, we achieved a 14.5% conversion efficiency with $V_{\text{oc}} = 613$ mV, $J_{\text{sc}} = 34.3$ mA cm^{-2} and FF = 0.689 for an active area of 0.23 cm^2 . The cross-sectional morphology of the films was examined by a field-emission scanning electron microscope (FESEM, JSM-6700F). The length scale of FESEM is about 1–10 μm , which is appropriate for investigating grain growth behaviors and the distribution of GBs. In particular, the cross-sectional view will lead to connectivity of the grains through the layer, which is a key factor in charge transport on the micrometer scale. Macroscopic chemical composition and crystal orientation were determined by inductively-coupled plasma (ICP) analysis and x-ray diffraction, respectively.

Raman scattering measurements were performed in the quasi-backscattering geometry by using a 632.8 nm line of a He–Ne laser (Mellis Griot, LHX2) as the excitation source. Scanning micro-Raman scattering measurements were carried out by focusing the excitation laser beam using a microscope objective with 50 of magnitude (0.8 numerical aperture) with a power of \sim 0.5 mW and collecting the scattered light in the backscattering geometry through the same objective. All the Raman spectra were collected with low intensity laser light to prevent thermal damage to the CIGS thin films. We performed line scans along the samples and obtained Raman image mappings with a scanning mode using a computer-controlled X–Y stage. Scattered light was filtered with two holographic edge filters, dispersed by an SPEX 0.32 m spectrometer and detected with a thermoelectrically-cooled back-illuminated charge-coupled-device (CCD) detector array. The full Raman spectrum at each position was accumulated for 5 s in steps of 250 nm, which were controlled by a motion controller. Spatial resolution of micro-Raman spectroscopy, which depends on the optics configuration, was about 1 μm or less. The merging of Raman imaging and topographical information will provide knowledge on charge transport, which is critically influenced by grain growth in polycrystalline solar cells.

In conductive atomic force microscopy (C-AFM) and Kelvin probe force microscopy (KPFM), the measurement configuration is a metal-coated tip on the CIGS films with Mo-coated glass. A Pt/Ir-coated cantilever was used for topographical and electrical measurements in the scanning probe experiments. A commercial AFM was used for the measurement (Nanofocus Inc., n-Tracer), which has a separate piezoelectric response between the XY-motion and the Z-approach. For the measurement of surface potential, KPFM was used in a non-contact mode at a resonant frequency of the probe of about 61.2 kHz and a scan rate of 0.5 Hz. Because of the low scan rate, the samples were not damaged in the course of taking these measurements, as demonstrated by the reproducibility of the topography and potential images. Current maps at a constant voltage were obtained at zero voltage and by applying 0.01 and 0.4 V onto the sample in a $1.2 \times 1.2 \mu\text{m}^2$ scanning area. The conducting probe was connected to ground and the current was detected with a single-terminal. Silver paste was used for the electrical contact in this measurement. The current was measured simultaneously with a contact mode. We set the same force of 1 nN on a probe and a scanning time of 500 ms for each line to obtain the local current. In order to reduce the impact of external factors on the local current during scanning, we also obtained the local current with various scan sizes and rates at a constant voltage. Even though it is not clear that tolerance of non-uniformity for physical properties is significant to photovoltaic efficiencies, mapping of the current and potential at the nanoscale is crucial for understanding the quality of the materials.

3. Results and discussion

3.1. Microstructure, crystallinity and grain growth

Surface and cross-sectional SEM images of the film are shown in figure 1. Figure 1(a) shows grains of about 1–2 μm in size

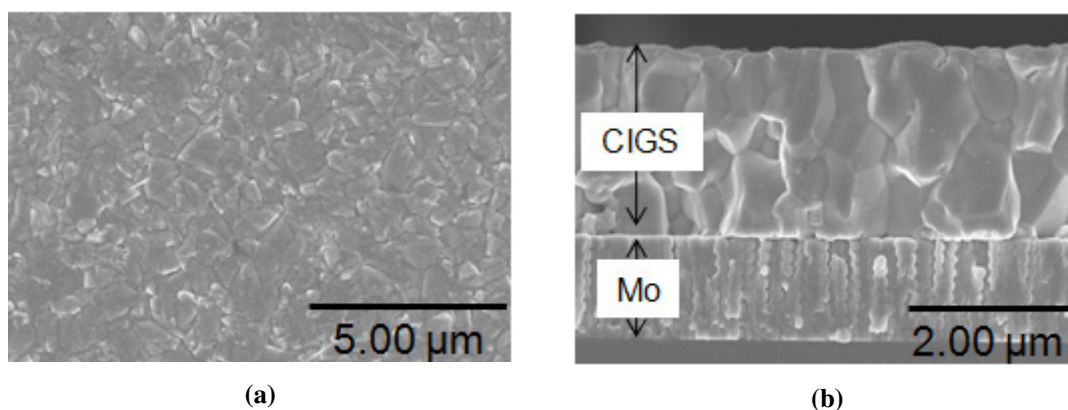


Figure 1. (a) Plane view and (b) cross-sectional images of scanning electron microscopy of a CIGS film on Mo substrate. The films have granular structure with a 1–2 μm grain size.

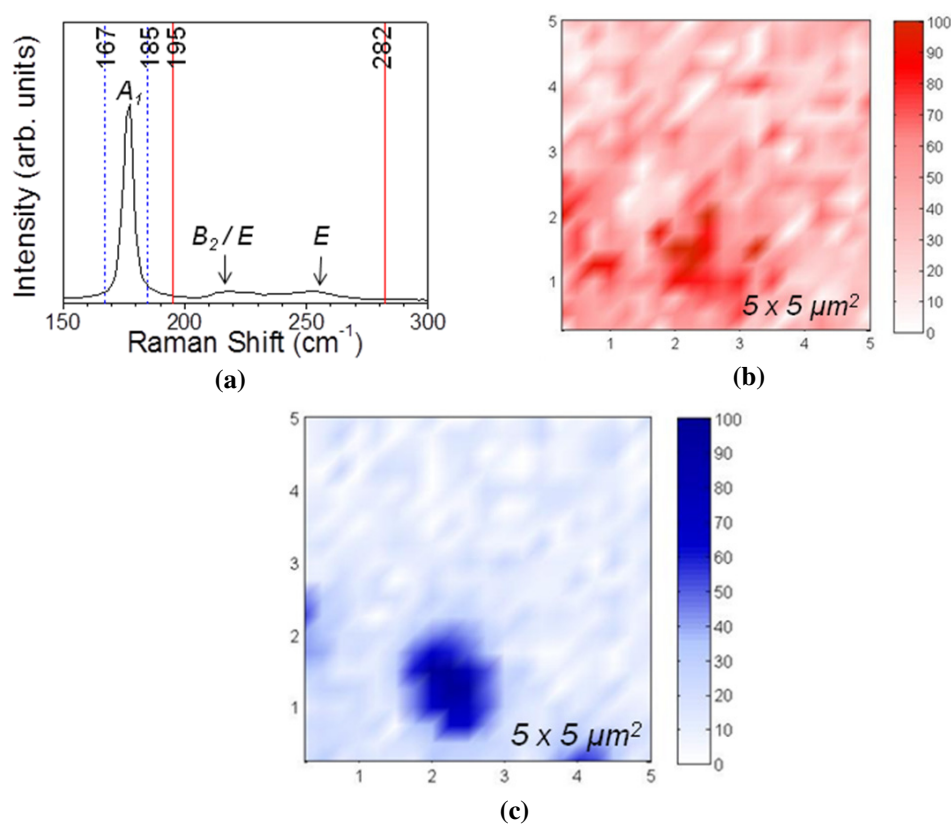


Figure 2. (a) Raman scattering spectrum of the CIGS film. The A_1 mode is shown at 175 cm^{-1} . The B_2 and E symmetry modes are also observed in the $195\text{--}282\text{ cm}^{-1}$ spectral region. Raman mappings of the spectral ranges (b) $167\text{--}187\text{ cm}^{-1}$ and (c) $195\text{--}282\text{ cm}^{-1}$. The scan size is $5 \times 5\ \mu\text{m}^2$.

and a compact growth on the surface. Figure 1(b) shows a cross-sectional image of the film with a columnar structure and a large grain size. The grains look very compact and tightly adhered to the Mo layer. The final average composition of the films are Cu/(In+Ga) and Ga/(In+Ga) ratios of approximately 0.9 and 0.3, respectively.

Figure 2 depicts the Raman spectrum and mapping of the CIGS films. In figure 2(a), the Raman spectrum shows a large A_1 mode, which represents the vibration of the Se anions in the $X\text{--}Y$ plane with the cations at rest [18]. The signal at $212\text{--}230\text{ cm}^{-1}$ is observed as a combination of B_2 and E modes from the vibrations of anions and cations together [18]. In addition to the B_2 and E modes, secondary phases like Cu_{2-x}Se are detected in a macroscopic measurement, which

are designated at $\sim 250\text{ cm}^{-1}$ [19–21]. Raman spectra images are shown in figures 2(b) and (c), which reveal clearly the distribution of the CIGS phases in a $5 \times 5\ \mu\text{m}^2$ area. Note that the mapping characterizes a region near the surface and not the whole thickness of the films. Figure 2(b) shows the distribution of the integrated intensity of the A_1 mode in the spectral range of $167\text{--}187\text{ cm}^{-1}$. The main A_1 mode is presented in the whole area although the intensity varies locally, which means the film has some non-uniformity on the surface. Figure 2(c), which is the image of the integrated intensity in the frequency region of $195\text{--}282\text{ cm}^{-1}$, gives information about the distribution of defects. The intensity of this region is very similar to that of the A_1 -mode distribution. The phonon vibrations from anions and cations together

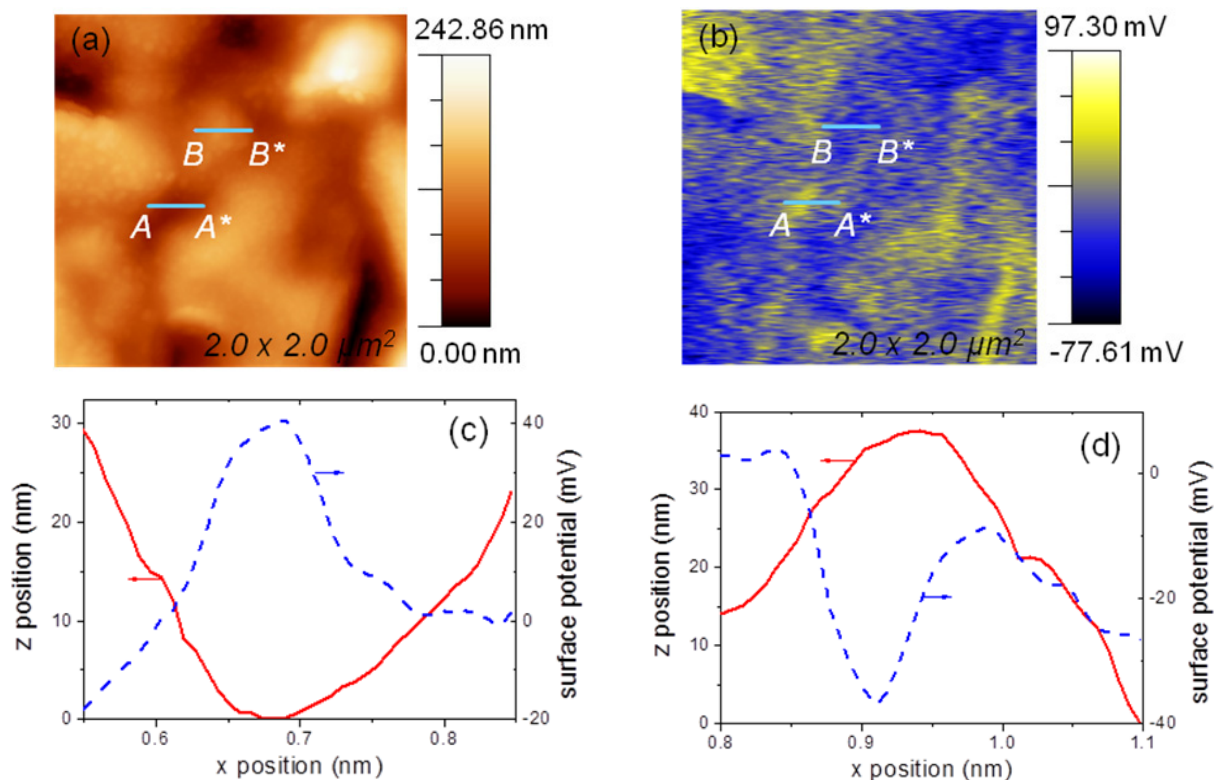


Figure 3. (a) Topography, (b) KPFM images of the CIGS film, (c) a line profile of the topography and KPFM signal from the region AA* from (a) and (b), (d) a line profile of the topography and KPFM signal for the region BB* from (a) and (b). The line scans display the measured height of the sample surface (left, red solid line) and the surface potential (right, blue dashed line). A peak of surface potential marks the position of a grain boundary in the same position of the sample, as shown in the bright regions in (b) and the line profile in (c).

co-exist with that from defects in the quaternary CIGS alloy in this region. From the Raman images, we could recognize that the CIGS thin film has crystalline variation and localized defects from local distribution. The Raman images are not continuous since the polycrystalline CIGS thin-film has different chemical compositions at each grain and GB. Thus, the phonon modes have locally distinct distributions.

3.2. Surface potential

Figure 3 shows the topography and surface potential of the CIGS film measured by KPFM. In this measurement, it is possible to get an absolute value for the spatial dimension and electric potential of the CIGS surface. In figure 3(a), the topography shows granular variations in a very small area. The detailed features of the grains were not observed in SEM observation, but the interior part of the grains and the deep gaps between the grains are displayed. The surface potential of the CIGS film looks more dramatic than the topography shown in figure 3(b). Some regions show negative potential but some show positive potential. It is easy to take notice of the potential variation associated with the topography. The surface potential at the GBs is higher than that between the grains, as shown in the bright region in the surface potential image in figure 3(c). The dark region in figure 3(b) indicates the lower surface potential at the high-grain interior, as shown in figure 3(d). The two-dimensional line profiles in figures 3(c) and (d) indicate exactly out-of-phase changes between the Z-position in topography and surface potential. The line scan of the surface potential had about 40 mV at the

GB while the surface potential at the grain interior is lower than that at the GB, showing negative values of approximately -37 mV inside the grains. The GBs of the CIGS film signify positively charged GBs with negative-conduction band bending. Jiang *et al* [9] reported the built-in potential at the GBs is beneficial for CIGS solar cell performance.

3.3. Current mapping

Figure 4 shows the topography and current mapping of the CIGS film measured by C-AFM in the dark at a low positive sample bias. The corresponding topographic image obtained at a contact mode is presented in figure 4(a). With the low external bias voltage, the dark current shows a positive value and is much higher at the GBs than elsewhere. In figures 4(b)–(f), the current mapping is shown as a function of external bias voltage. Dark current starts to flow more at the GBs than in the grain interiors under very low external bias from 0.01 to 0.04 V (figures 4(b)–(d)). As the external bias voltage increased from 0.1 to 0.4 V, the current is positively enhanced at the GBs. Inside the grains, the corresponding field does not induce significant current, possibly due to a more abrupt recombination at the grain interior than at the GBs [22]. The behavior of the GB barriers is consistent with the KPFM results shown in figure 3. It is found that current flowing along the GBs reaches a compliance limit of 8 nA and gradually exceeds that even through the grain interiors at external bias voltages of 0.1 and 0.4 V, as shown in figures 4(e) and (f), respectively.

Figures 5(a)–(e) indicate the three-dimensional current routes of each image from the current mapping in figure 4.

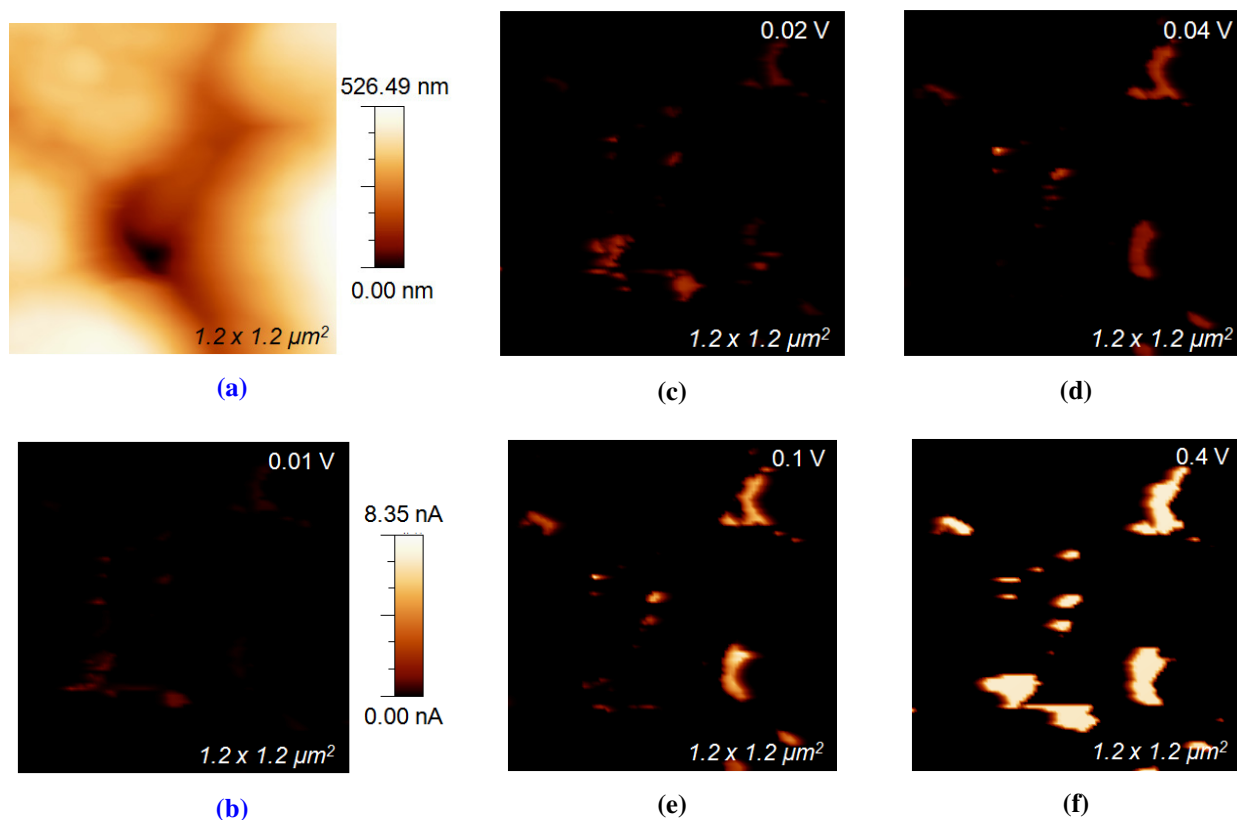


Figure 4. (a) Topography of CIGS films. Grains and grain boundaries are shown in this topography. Current maps of the CIGS films with external bias: (b) 0.01, (c) 0.02, (d) 0.04, (e) 0.1 and (f) 0.4 V. The current reaches a compliance value when the bias is close to 0.4 V.

A valence band offset of 0.3–0.4 eV is known according to the theoretical predictions [21, 23–25]. Local current increases as the external bias voltage increases. In figure 5(e), the local current value reached 8 nA under 0.4 V, as mentioned in the previous paragraph and described in figure 4(f). Electrons flow gradually increases to surpass the valence-band offset. The local current increases only along the Z-direction below 0.1 V, but then begins to broaden laterally above 0.4 V, as shown in figure 5(e). As the external bias is increased to 0.4 V, the local current is enhanced to a greater extent laterally in the entire region, indicating that the current flows not only through the GBs but also inside the grains.

3.4. Defects and charge transport

A defect state is known to exist in the band gap caused by $V_{\text{Se}}-V_{\text{Cu}}$ in the donor configuration, which is considered to be a metastable defect in the CIGS materials [26]. As the external bias voltage increases, electrons are injected. The activated capture of one electron leads to the electron–hole exchange reaction at the vacancy sites of Se and Cu, where the complex of the vacancies converts the donors to the acceptors configuration. This reaction brings about an increase in the net acceptor concentration of the p-type CIGS absorber [20]. The electrons injected by external bias go through the increased acceptor level and are trapped. For a p-type CIGS, $(V_{\text{Se}}-V_{\text{Cu}})^+$ state exists in donor configuration with the lowest energy [26]. At a very low external bias of less than 0.2 V, a relatively low density of electrons is trapped by the $(V_{\text{Se}}-V_{\text{Cu}})^+$ divacancies. It leads to the low and gradually increased current flow.

On the other hand, when higher bias than the valence-band offset was induced, excessive electrons filled the divacancies, abruptly flow and result in laterally increased local current. This suggests that divacancies may not be able to trap lots of electrons as many more electrons are injected. Consequently, the number of electrons that move from the valence band to the conduction band gradually increases laterally, depending on the external bias. Since the conduction band of the GB is bent downward owing to positively charged GBs as described in the KPFM results and the electron–hole separates at the GBs, it also reinforces the current routes at the GBs.

Judging from the local electrical properties, we can suggest a potential diagram without external bias as shown in figure 6(a). When a p-type semiconductor CIGS contacts with a Pt metal using as an AFM tip, the band is bent downward around the interface. With the typical E_F-E_V of ~ 200 in the polycrystalline CIGS materials [15, 27], it is found that several tens of the mV band-bending and 300–400 meV of valence-band offset occurred. The potential diagram presented in figure 6(a) is consistent with our results, which indicate charge separation at the GBs that are not recombination centers. In the schematic band diagram of figure 6(b), the band is less downward after positive bias voltage was applied. In figure 6(a), the conduction band (~ 40 meV) and valence band offset (~ 300 meV) at the GBs are designated. As the external bias increases, the depletion region between semiconductor CIGS and Pt metal is shorter than that of non-bias owing to the reduced downward band as shown figure 6(b). Thus, it helps electron transport and brings about increase of current flow under higher external

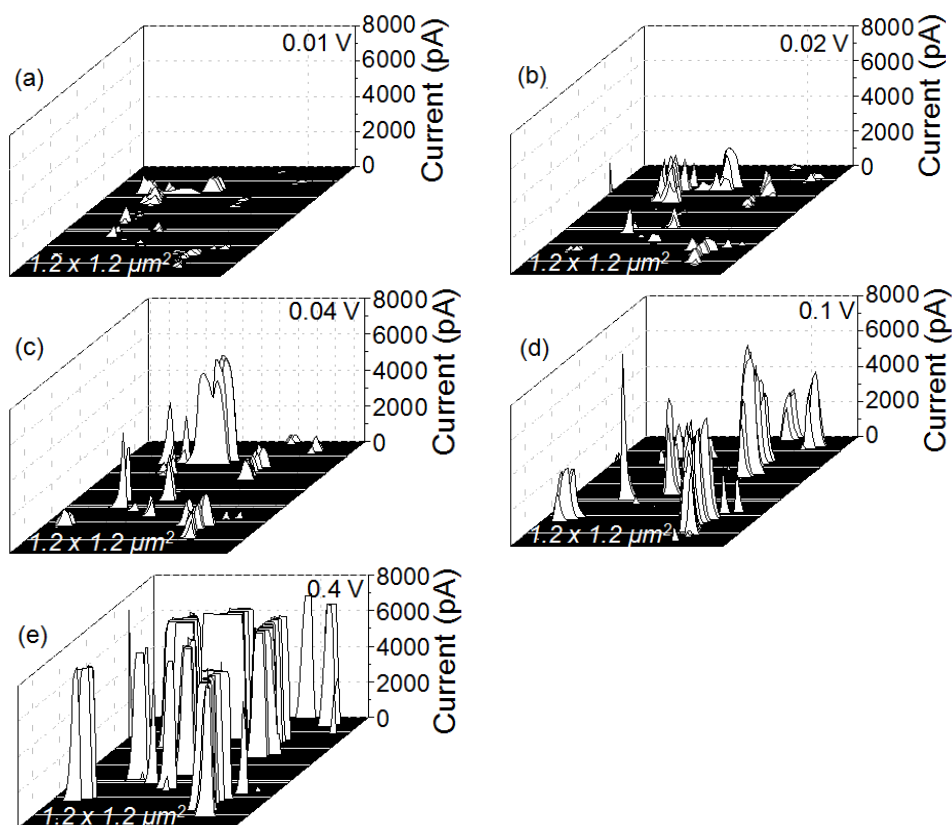


Figure 5. Line profiles of the topography and current mapping from figure 4. (a) $V = 0.01$, (b) 0.02 , (c) 0.04 , (d) 0.1 and (e) 0.4 V of external bias. They also prove that the current was higher around grain boundaries and enlarged laterally.

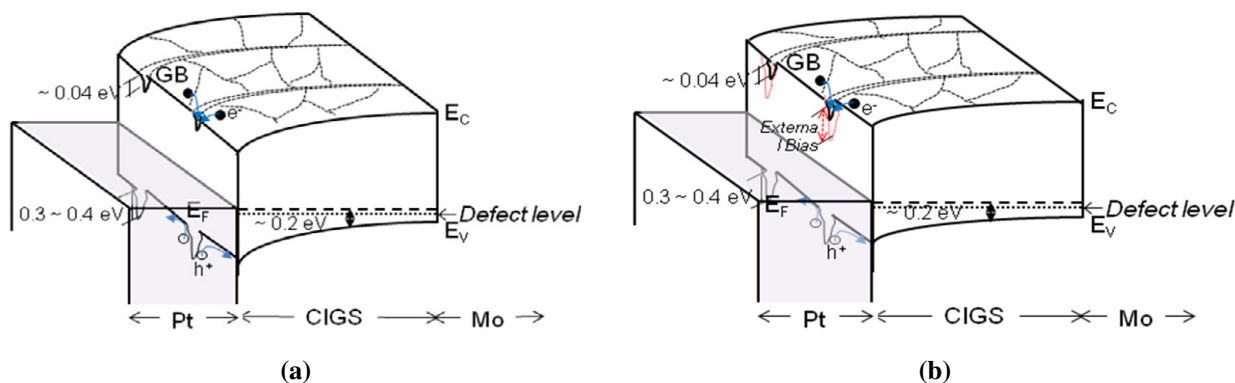


Figure 6. Schematic band diagram representation of the conduction and valence bands in the CIGS layer at the GBs that can account for most of the electron transport at the GBs (a) in the dark and with non-external bias and associated with the features seen in the KPFM and C-AFM measurements. (b) As the external bias increases, the reduced downward band leads to a shorter depletion region and helps electron transport. Near GBs, the local built-in potential attracts electrons and repels holes, which is the advantage of solar cell properties.

bias voltages. It is also shown that polycrystalline CIGS is not homogeneous in bulk judging from Raman spectra imaging. Local electrical properties tend to behave similarly throughout most of the surface region, indicating that the positively charged GB attracts electrons and repels holes from the GB.

4. Conclusion

Surface imaging and mapping of the microstructure and electrical properties of a CIGS film demonstrate that the polycrystalline thin film is not homogeneous in composition and structure, but efficiency-favorable charge transport is

dominant near the GBs. Raman spectra images of the CIGS film are used to identify the distribution of composition and structure where intensive A_1 of the CIGS phase and B_2/E or other defect phases are obtained. Electrical properties measured at the nanoscale imply that the surface potential and current are dependent on grains and GBs. The GBs are positively charged and repel holes from GBs and attract electrons. The conduction mechanism leading to improved performance in polycrystalline CIGS solar cells was also suggested. We conclude that identifying local chemical and structural properties is essential for improving the absorber layer despite inhomogeneous polycrystalline thin

films, as well as determining local electrical properties for understanding electron–hole behavior in the absorber layer.

Acknowledgments

This work was supported by the New and Renewable Energy Technology Development Program of the Korea Institute of Energy Technology Evaluation and Planning (KETEP) grant funded by the Korea Government Ministry of Knowledge Economy (no. 20113020010040) and supported by the DGIST R&D Program of the Ministry of Education, Science and Technology of Korea (11-BD-01).

References

- [1] Chopra K L and Das S R 1983 *Thin Film Solar Cells* (New York: Plenum) pp 417–22
- [2] Dhere N D 2007 *Sol. Energy Mater. Sol. Cells* **91** 1376
- [3] Green M A 2007 *J. Mater. Sci., Mater. Electron.* **18** S15
- [4] Repins I, Contreras M A, Egaas B, DeHart C, Scharf J, Perkins C L, To B and Noufi R 2008 *Prog. Photovolt. Res. Appl.* **16** 235
- [5] Boiso A, Romeo N, Podesta A, Mazzamuto S and Canevari V 2005 *Cryst. Res. Technol.* **40** 1048
- [6] Champness C H 2002 *Proc. Specialist Conf. on 29th IEEE Photovoltaic (New Orleans, 2002)* (Piscataway, NJ: IEEE) p 732
- [7] Yan Y, Jiang C-S, Noufi R, Wei S-H, Moutinho H R and Al-Jassim M M 2007 *Phys. Rev. Lett.* **99** 235504
- [8] Hetzer M J, Stzhemechny Y M, Gao M, Contreras M A, Zunger A and Brillson L J 2005 *Appl. Phys. Lett.* **86** 162105
- [9] Jiang C-S, Noufi R, Abushama J A, Ramanathan K, Moutinho H R, Pankow J and Al-Jassim M M 2004 *Appl. Phys. Lett.* **84** 3477
- [10] Monig H, Smith Y, Caballero R, Kaufmann C A, Lauermann I, Lux-Steiner M Ch and Sadewasser S 2010 *Phys. Rev. Lett.* **105** 116802
- [11] Hafemeister M, Siebentritt S, Albert J, Lux-Steiner M Ch and Sadewasser S 2010 *Phys. Rev. Lett.* **104** 196602
- [12] Medvedkin G A, Terukov E I, Hasegawa Y, Hirose K and Sato K 2003 *Sol. Energy Mater. Sol. Cells* **75** 127
- [13] Merdes S, Mainz R, Klaer J, Meeder A, Rodriguez-Alvarez H, Schock H W, Lux-Steiner M Ch and Klenk R 2011 *Sol. Energy Mater. Sol. Cells* **95** 864
- [14] Hanna G, Glatzel T, Sadewasser S, Ott N, Strunk H P, Rau U and Werner J H 2006 *Appl. Phys. A* **82** 1
- [15] Dullweber T, Hanna G, Rau U and Schock H W 2001 *Sol. Energy Mater. Sol. Cells* **67** 145
- [16] Wada T, Hashimoto Y, Nishiwaki S, Satoh T, Hayashi S, Negami T and Miyake H 2001 *Sol. Energy Mater. Sol. Cells* **67** 305
- [17] Rau U, Braunger D, Herberholz R, Schock H W, Guillemoles J F, Kronik L and Cahen D 1999 *J. Appl. Phys.* **86** 497
- [18] Tanino H, Maeda T, Fujikake H, Nakanishi H, Endo S and Irie T 1992 *Phys. Rev. B* **45** 13323
- [19] Weszka J, Daniel P, Burian A, Burian A M and Nguyen A T 2000 *J. Non-Cryst. Solids* **265** 98
- [20] Ramdani O, Guillemoles J F, Lincot D, Grand P, Chassaing E, Kerrec O and Rzepk E 2007 *Thin Solid Films* **515** 5909
- [21] Persson C and Zunger A 2003 *Phys. Rev. Lett.* **91** 266401
- [22] Kronik L, Rau U, Guillemoles J F, Braunger D, Schock H W and Cahen D 2000 *Thin Solid Films* **361** 353
- [23] Persson C and Zunger A 2005 *Appl. Phys. Lett.* **87** 211904
- [24] Gloeckler M, Sites J R and Metzger W K 2005 *J. Appl. Phys.* **98** 113704
- [25] Wei S-H and Zhang S B 2005 *J. Phys. Chem. Solids* **66** 1994
- [26] Lany S and Zunger A 2006 *J. Appl. Phys.* **100** 113725
- [27] Azulay D, Millo O, Balberg I, Shock H W, Visory-Fisher I and Cahen D 2007 *Sol. Energy Mater. Sol. Cells* **91** 85